Nanoscale

Large-Area 2D PtTe2/Silicon Vertical-Junction Devices with Ultrafast and High-Sensitivity Photodetection and Photovoltaic Enhancement by Water Droplet

Journal:	*Nanoscale*
Manuscript ID	NR-ART-07-2020-005670.R1
Article Type:	Paper
Date Submitted by the Author:	08-Oct-2020

Complete List of Authors:	Shawkat, Mashiyat ; University of Central Florida, NanoScience Technology Center Chowdhury, Tanvir Ahmed; University of Central Florida, NanoScience Technology Center Chung, Hee-Suk; Korea Basic Science Institute, Sattar, Shahid; KAUST, MSE Ko, Tae-Jun ; University of Central Florida, NanoScience Technology Center Larsson, Andreas; Applied Physics, Division of Materials Science, Engineering Sciences and Mathematics; Tyndall National Institute, Theory, Modelling and Design Jung , Yeonwoong; University of Central Florida, Materials Science & Engineering

ARTICLE

Large-Area 2D $PtTe_2$/Silicon Vertical-Junction Devices with Ultrafast and High-Sensitivity Photodetection and Photovoltaic Enhancement by Water Droplet

Mashiyat Sumaiya Shawkat,[a, b] Tanvir Ahmed Chowdhury,[c] Hee-Suk Chung,[d] Shahid Sattar,[e] Tae-Jun Ko,[a] J. Andreas Larsson,[e] and Yeonwoong Jung*[a, b, f]

2D $PtTe_2$ layers, a relatively new class of 2D crystals, exhibit unique band structure and remarkably high electrical conductivity promising for emergent opto-electronics. This intrinsic superiority can be further leveraged toward practical device applications by merging them with matured 3D semiconductors, which has remained largely unexplored. Herein, we explored 2D/3D heterojunction devices by directly growing large-area (>cm^2) 2D $PtTe_2$ layers on Si wafers using a low-temperature CVD and unveiled their superior opto-electrical characteristics. The devices exhibited excellent Schottky transports essential for high-performance photovoltaics and photodetection; i.e., well-balanced combination of high photodetectivity (>10^{13} Jones), small photo-responsiveness time (~1μs), high current rectification ratio (>10^5), as well as water super-hydrophobicity driven photovoltaic improvement (>300%). These performances were identified to be superior to those of previously explored 2D/3D or 2D layers-based devices with much smaller junction areas, and their underlying principles were clarified by DFT calculation.

Introduction

Recently, interests in a family of noble metals-based two-dimensional (2D) crystals are on the rise exploiting their superior electrical properties beyond conventional 2D transition metal dichalcogenides (TMDs).[1-5] While a large number of semiconducting 2D TMD layers have been explored for unconventional opto-electronics,[6, 7] their carrier mobility values still remain uncompetitive with those of traditional semiconductors.[8, 9] In this regard, noble metals (particularly, platinum (Pt))-based ones offer distinguishable advantages of high carrier mobility[10-15] and air-stability even better than black phosphorus (BP) as well as low-temperature synthesis.[16, 17] 2D platinum ditelluride ($PtTe_2$) layers are a recent addition to them and present a large set of unparalleled properties beyond other Pt-based 2D TMD layers.[18-20] Most notably, they exhibit an extremely high electrical conductivity of > 10^6 S/m - superior to most of previously reported 2D TMD layers, which is well maintained even with scalable wafer-level growths.[1, 21-23] Such intrinsic superiority is projected to be further promoted when they are merged with conventional 3D semiconductors yielding well-controlled 2D/3D heterojunctions, particularly for opto-electronic applications.[24] In general, such 2D/3D heterojunctions exist in two distinct configurations, i.e., lateral vs. vertical, determined by the ways that 2D layers are interfaced with the 3D materials. While laterally integrating small-sized 2D flakes onto 3D semiconductors has accomplished high photosensitivity, the resulting devices exhibited limited photo-response speeds in the range of few-to-milli-seconds.[25-27] The vertical integration approach would offer advantages of small diffusion length and depletion dimensions for photo-generated carriers, therefore, faster photo-responsiveness. However, it remains difficult to achieve 2D/3D vertical junctions on a laterally large (~cm^2) dimension *via* a scalable process avoiding the unreliable manual transfer of 2D layers.[28, 29] Herein, we fabricated large-area (~cm^2) $PtTe_2$/Si 2D/3D vertical heterojunction devices by directly growing metallic 2D $PtTe_2$ layers on pre-patterned Si wafers using a scalable chemical vapor deposition (CVD) method. We unveiled their "intrinsically" superior photovoltaic and photodetection performances over previously explored devices as well as identifying methods to "externally" further promote such superiority.

Experimental

Device fabrication

300 nm SiO_2 was deposited on a cleaned Si wafer through a shadow mask at a rate of 1 $Å/s$ by electron-beam evaporation (Thermionics VE-100). Pt film was deposited on the prepared SiO_2/Si wafer through another shadow mask at a rate of 0.05

[a] NanoScience Technology Center, University of Central Florida, Orlando, Florida 32826, USA. E-mail: yeonwoong.jung@ucf.edu
[b] Department of Electrical and Computer Engineering, University of Central Florida, Orlando, Florida 32816, USA.
[c] Department of Mechanical and Aerospace Engineering, University of Central Florida, Orlando, Florida 32816, USA.
[d] Analytical Research Division, Korea Basic Science Institute, Jeonju 54907, South Korea.
[e] Applied Physics, Division of Materials Science, Department of Engineering Sciences and Mathematics, Luleå University of Technology, Luleå SE 97187, Sweden.
[f] Department of Materials Science and Engineering, University of Central Florida, Orlando, Florida 32816, USA.
† Footnotes relating to the title and/or authors should appear here.
Electronic Supplementary Information (ESI) available: [details of any supplementary information available should be included here]. See DOI: 10.1039/x0xx00000x

$\text{Å}/s$, defining Pt/Si active and Pt/SiO_2 electrode areas. The prepared sample was transferred to the middle of a quartz tube CVD furnace, and Te powders were placed in an alumina boat at the furnace upstream side. The tube was purged with Argon (Ar) gas and pumped down to a base pressure of ~1 mTorr. The furnace temperature was ramped up to 400 ℃ in 50 mins and then maintained at the temperature for another 50 mins. Throughout the reaction, Ar gas was constantly flowed (100 SCCM) through the tube, maintaining its operation pressure at ~80 mTorr. Once the $PtSe_2/SiO_2/Si$ samples were prepared, Au electrodes (50 nm thickness) were deposited through another shadow mask using Quorum Q150T Plus sputtering system.

TEM and Raman characterization

Microstructure analysis of 2D $PtTe_2$ layers was performed with a JEOL ARM 200 F Cs-corrected TEM at an operation voltage of 200 kV. For the plane-view TEM characterization of 2D $PtTe_2$ layers, we directly grew them on a SiO_2/Si wafer and applied buffered oxide etchant (BOE) to the as-grown 2D $PtTe_2$ layers-SiO_2/Si sample. The BOE gently etched away the underlying SiO_2, lifting off the 2D $PtTe_2$ layers only. The delaminated 2D $PtTe_2$ layers were transferred onto copper TEM grids. For the cross-sectional TEM sample preparation, focused ion beam (FIB; Quanta 2D FEG, FEI)-based milling and lift-out techniques were employed. For Raman spectroscopy characterization, Renishaw RM 1000B system with a laser source of 514 nm wavelength was used.

Electrical and photovoltaic characterization

All electrical measurements were performed with a home-built probe station using a HP 4156 A semiconductor parameter analyzer. Photovoltaic measurements were carried out using an AM 1.5 solar simulator (G2V optics). Photo-response measurements were carried out using M625L4-C2 – 625 nm Thorlabs LED. The response speed was characterized using a home-built measurement system using Tektronix MDO4104C digital oscilloscope. The frequency modulation of the LED source was carried out using Tektronix AFG 3022C function generator.

Water contact angle measurement

Water contact angles of 2D $PtTe_2$ layers were measured with a goniometer (model 90, Ramé-Hart instrument co.). Water droplets (2 µL) were gently integrated on the surface of as-grown 2D $PtTe_2$ layers using a micro-syringe, and the contact angle values were extracted using the DROPimage Pro software (Ramé-Hart instrument co.).

Results

Fig. 1 presents the preparation of $PtTe_2/Si$ devices and the structural/chemical characterization of the adopted 2D $PtTe_2$ layers. **Fig. 1a** illustrates the sequential procedures for the device fabrication, starting with the patterned deposition of silicon dioxide (SiO_2) on p- doped Si wafers (resistivity ~1-5 Ωcm). Pt thin films of controlled thickness are selectively deposited on the wafers *via* an electron beam evaporator using a shadow mask. Subsequently, 2D $PtTe_2$ layers are grown at 400 ℃ through the CVD tellurization method developed in our previous studies,[1, 23] defining the lateral dimension of $PtTe_2/Si$ vertical heterojunctions. Lastly, gold (Au) electrodes are selectively deposited on the top $PtTe_2/SiO_2$ side as well as the wafer bottom side. Details for the sample preparation are presented in the *Experimental section*. **Fig. 1b** shows a representative image of a complete $PtTe_2/Si$ device with Au electrodes. **Fig. 1c** shows a Raman spectroscopy characterization of few-layer 2D $PtTe_2$ obtained by the CVD tellurization of Pt ~0.3 nm, comparing experimentally determined (blue dotted line) vs. theoretically calculated (black solid line) characteristics. Two characteristic peaks of E_g and A_{1g} are noted, where E_g (A_{1g}) peaks depict the in-plane (out-of-plane) vibrational modes of Te atoms within the 2D layers, respectively. Excellent agreement is observed between these two spectra of experimental vs. theoretical in terms of their peak positions. The atomic crystallinity of the CVD-grown 2D $PtTe_2$ layers were studied using a scanning transmission electron microscope (STEM). **Fig. 1d** presents a dark-field STEM image of as-grown 2D $PtTe_2$ layers, unveiling a large number of polycrystalline grains. Each grain is individually "stitched" with respect to its neighbouring ones, achieving a high spatial homogeneity over the entire sample area. The inset in **Fig. 1d** is the corresponding selective area diffraction (SAED) pattern, showing a dominant appearance of (110) $PtTe_2$ plane.[1] **Fig. 1e** shows a plane-view high-resolution (HR) STEM image of the polycrystalline 2D $PtTe_2$ layers, revealing two adjacent stitching grains separated by the grain boundary (purple curve). Each grain exhibits distinguishable Moiré fringes, indicating vertical stacking of individual 2D layers with misaligned crystallographic orientation. **Fig. 1f** shows a cross-sectional HRSTEM image to reveal well-defined van der Waals (vdW) gaps in vertically-stacked 2D $PtTe_2$ layers, indicating their layer-by-layer growth. **Fig. 1g** shows the corresponding energy-dispersive X-ray spectroscopy (EDS) elemental map images, unveiling spatial homogeneity of constituent elements.

Fig. 2 presents electrical properties of stand-alone 2D $PtTe_2$ layers as well as $PtTe_2/Si$ heterojunction devices. CVD-2D $PtTe_2$ layers exhibit extremely high electrical conductivity of ~10^5–10^6 S/m and intrinsically metallic transports irrespective of their layer numbers, as verified in our previous studies.[1] For further clarification, we characterized their transport properties in field effect transistor (FET) configurations, and confirmed no noticeable gate responses (**Fig. S1, ESI†**). Additionally, we identified their electronic band structure by density functional theory (DFT) calculation[30] and verified strong metallic dispersion characteristics (**Fig. S2, ESI†**). Having confirmed the highly metallic nature of 2D $PtTe_2$ layers, we developed the heterojunction devices by optimizing their layer thickness. **Fig. 2a** shows the photovoltaic characterization of a device incorporating 2D $PtTe_2$ layers prepared with Pt of ~4.5 nm thickness, revealing the current density – voltage (J-V)

characteristics without (red) and with (blue) a solar illumination (intensity: 400 W/m^2). The device displays pronounced photovoltaic effects corroborated by the large amount of photo-induced current density at the reverse bias regime. **Fig. 2b** presents the corresponding J-V plot in a semi-log scale, yielding following parameters; open circuit voltage (V_{oc}) ~ 0.41 V, short circuit current density (J_{sc}) ~5.9 mA/cm^2, fill factor (FF) ~44%, and rectification ratio ~10^5 at ± 1.5V. The device ideality factor, *n*, extracted from the linearity (black line) in the forward bias regime is ~1.9 and the power conversion efficiency (PCE) is ~2.5 %. This observation of strong current rectification and photovoltaic characteristics confirms a presence of metal ($PtTe_2$)-semiconductor (Si) Schottky junctions whose mechanism will be discussed in the next section. Additionally, we confirmed Ohmic transport characteristics from 2D $PtTe_2$ layers and p-Si wafers interfaced with Au electrodes (**Fig. S3, ESI†**), which further verifies that the rectification originates from the junctions. Representative data obtained from the devices prepared with smaller (~0.3 nm) and larger (~13.5 nm) Pt thickness are presented in **Fig. S4, ESI†**, confirming inferior performances compared to the optimized one. This thickness-sensitive photovoltaic performance is attributed to the competing effect of thickness-dependent optical transmittance vs. electrical conductivity as verified in our previous studies.[1, 23]; the optical transmittance steeply decreases with increasing thickness while the electrical properties are less thickness-sensitive exhibiting a maximum conductivity at a certain thickness due to the anisotropic crystallinity of 2D $PtTe_2$ layers.[1, 23] We note that these $PtTe_2$/Si heterojunction devices perform much better than the previously explored Pt TMD-based ones including platinum diselenide ($PtSe_2$)/Si of comparable thickness,[12]; i.e., increase of ~15% and ~47% for V_{oc} and J_{sc}, respectively. In addition to photovoltaics, we also investigated their photo-responsiveness using an illumination source of a fixed wavelength. **Fig. 2c** shows semi log-scaled I-V characteristics of another device different from the one for **Fig. 2a** and **2b** under intensity-varying illumination at 625 nm wavelength. The photocurrent at the reverse bias regime steadily increases with increasing intensity, reflecting the increasing concentration of photo-generated charge carriers.[31] **Fig. 2d** shows a time-dependent train of photocurrent generation at a zero external bias under periodic illumination of varying intensity revealing highly reliable photo-responsiveness. We also confirmed that the device was still very sensitive even at a much lower intensity of 0.1 mW/cm^2 (**Fig. S5, ESI†**). Photo-responsivity and specific detectivity are two key parameters used to evaluate the photo-responsiveness performance of the device; Photo-responsivity, *R*, indicates its efficiency in responding to changes in optical signals, whereas the specific detectivity, D^*, delineates its ability to detect small signals. They are obtained from the following equations;[32, 33]

$$R = \frac{I_{ph}}{P_{in}} \quad (1)$$

$$D^* = \frac{A^{\frac{1}{2}}R}{(2eI_d)^{\frac{1}{2}}} \quad (2)$$

where I_{ph}, I_d, P_{in}, A and e are the photocurrent, dark current, incident light power, active device area, and elementary charge, respectively. **Fig. 2e** presents plots of *R* (blue) and D^* (red) vs. light intensity extracted from the above equations for the $PtTe_2$/Si device at a zero external bias. Both *R* and D^* show inverse relationship with intensity, consistent with the observations with other 2D/3D photodetectors.[31, 34, 35] The *R* value reaches up to 0.213 A/W at 1.1 mW/cm^2, comparable to those of other 2D/3D photodetectors at a zero external bias.[32, 35, 36] Furthermore, the D^* value is as high as 2.66×10^{13} Jones, which is much higher than those of previously developed 2D/3D and stand-alone 2D devices – to be verified in the next section. This finding is particularly encouraging given that the lateral dimension of the active junction area in our device is quite large (1 cm × 0.5 cm) while previous developments mostly employed small-sized (typically, ~μm^2) exfoliated 2D flakes. Additionally, the external quantum efficiency (EQE) of the device was extracted using the following equation;

$$\text{EQE} = \frac{hcR}{e\lambda} \quad (3)$$

which yields a moderately high ECE of 42.2 %. In the above equation, h is the planck's constant, c is the velocity of light, R is the responsivity, and λ is the wavelength of the illumination source. Key parameters of various 2D/3D photodetectors operated at a zero bias are compared and presented in Table 1, **ESI†**. It is noted that the perfomance of our $PtTe_2$/Si device is comparable to those of the previously explored ones despite its much larger junction area.

Furthermore, we studied the practical suitability of the $PtTe_2$/Si device for high-performance photodetection applications. Particularly, photo-response speed is of paramount importance in optical communication and imaging applications as it dictates their efficiency for optical-to-electrical signal conversion. For the precise quantification of response speed, a 625 nm wavelength light was pulsed and introduced to the device using a signal generator as demonstrated in **Fig. 3a**. The temporal photo-response of the device at a zero external bias was recorded using a digital oscilloscope at several frequencies. **Fig. 3b-d** present the normalised transient photocurrents generated by the pulsed illumination with frequencies of 10 Hz, 30 kHz and 300 kHz, respectively. The results show well-resolved and retained photo-responsiveness even up to a very high frequency of 300 kHz for multiple cycles, confirming fast and reliable photo-switching. **Fig. 3e** presents the relative current balance of the device, i.e., $(I_{max}-I_{min})/I_{max}$, as a function of the modulation frequency where I_{max} (I_{min}) is the maximum (minimum) current obtained at each frequency with (without) illumination over multiple cycles, respectively. A high balance of >95 % is well preserved up to a frequency of 100 kHz, after which it steadily attenuates with increasing frequencies. This current attenuation still maintains ~80.6 % of its maximum even at a very high frequency of 300 kHz, significantly surpassing the 3-db cut-off frequency standard in commercial applications[37, 38] as well as the values observed with previously developed 2D/3D devices.[32, 33, 39] **Fig. 3f** shows a representative plot of the photocurrent generation/decay transient characteristics obtained at 150 kHz,

quantifying photo response intervals. The rise (τ_r) and fall (τ_f) times are determined from the 90% and 10% of the maximum current value, respectively, yielding τ_r ~1.68 µs and τ_f~1.58 µs. Comparison is made between the $PtTe_2$/Si device vs. previously developed 2D layers-based devices in terms of photo-detectivity and response time, as shown **Fig. 3g**. What is noteworthy is that this $PtTe_2$/Si device exhibits well-balanced characteristics of high photo-detectivity and fast photo-responsiveness; while the responsitivity, *R,* is observed to be similar in the measured wavelength range (~600 - 850 nm)[32-34, 36, 38-43], both the response time and photo-detectivity are much better than those observed with most of 2D/3D, 2D/2D, and stand-alone 2D layers-based devices.[27, 28, 33, 34, 39, 41, 44-55] This is particularly encouraging given the large (~0.5 cm^2) lateral dimension of the $PtTe_2$/Si junction enabled by the scalable CVD growth, while a large number of the previously developed ones are based on the manual integration of small-sized 2D flakes.[26-29, 41, 45, 47, 54, 56, 57]; For instance, although the graphene/Si device[29] in **Fig. 3g** exhibits slightly faster photo-response, its active junction area is only ~0.25 mm^2 which is 200 times smaller than ours. Furthermore, the $MoTe_2$/Si device[35] in **Fig. 3g** slightly outperforming our device demanded a manual integration of additional graphene top layers, thus limiting its process scalability.[43] Meanwhile, our $PtTe_2$/Si devices exhibit "intrinsic" 2D/3D Schottky junction characteristics un-aided by any additional materials and processes preserving a low-temperature growth scalability.

To clarify the charge transport mechanism of the device, we study the $PtTe_2$/Si heterojunction contact characteristics by theoretically determining its Schottky barrier height using first principle calculations. The planar average electrostatic potential (PAEP) of the $PtTe_2$/Si interface is computed in the out-of-plane direction along Si (100) orientation, as presented in **Fig. 4a**. The work function of few-layer 2D $PtTe_2$, Φ_M, is defined as $\Phi_M = E_{vac} - E_{Fermi}$, where E_{vac} is the vacuum level set to 0 eV to calibrate the energy scale, and E_{Fermi} is the highest occupied electron energy state at 0 K.[58] The work function value is determined to be ~ 4.56 - 4.57 eV with the layer number ranging from three to six. We also computed the band offset and the work function of p-Si by superimposing the PAEP of bulk Si on that of the slab (**Fig. S6, ESI†**). The PAEP diagram in **Fig. 4b** shows the work function of p-Si, Φ_{Si} is ~ 4.95 eV, determined from the experimental bandgap (~1.1 eV) of Si. Since the work function of the metallic 2D $PtTe_2$ layers is smaller than that of p-Si, a p-type Schottky junction is anticipated to form when these two materials are interfaced, as depicted in **Fig. 4c**. To determine the Schottky barrier height, Φ_b, for this junction, we refer to the known equation, $\Phi_b = E_g + \chi - \Phi_M$,[59] where E_g (~1.1 eV) is the bandgap and χ (~4.13 eV) is the electron affinity of Si, and Φ_M is the work function of 2D $PtTe_2$ layers. We identify that 2D $PtTe_2$ layers form an obvious Schottky junction, yielding Φ_b= 0.67 eV. **Fig. 4d** describes a diagram of the energy band bending at the $PtTe_2$/p-Si interface, which strongly justifies that the experimentally observed characteristics are a result of 2D/3D Schottky junctions. In the diagram, E_c, and E_V represent the conduction and valence band edge of Si, respectively. Details for the computational method are presented in *Computational section* (**ESI†**). We also determined the Φ_b value by analysing experimentally obtained I-V characteristics and observed good agreement with the theoretically calculated one (**Fig. S7, ESI†**).

Lastly, we demonstrated externally tunable opto-electrical properties in the $PtTe_2$/Si devices by taking advantage of the intrinsic structural uniqueness of 2D $PtTe_2$ layers. We identified that the large-area 2D $PtTe_2$ layers intrinsically exhibit "super-hydrophobic" surfaces as manifested by the very large (> 110°) water contact angle shown in **Fig. 5a**. Indeed, this hydrophobicity is highest among all previously explored 2D TMD layers[60, 61], which can be exploited to further improve device performances as presented in **Fig. 5b-5g. Fig. 5b** shows representative I-V characteristics of an identical $PtTe_2$/Si device in three different conditions; i.e., in dark (blue), under illumination (red), as well as under the same illumination with water droplets integration (black) which drastically improved the photovoltaic effect as manifested by the significant increase of reverse current. **Fig. 5c** shows the corresponding semi-log scaled I-V characteristics, better visualizing the photovoltaic enhancement. **Fig. 5d** summarizes the water droplet-driven change of photovoltaic parameters, revealing enhancements of J_{sc} by ~309%, V_{oc} by ~9%, PCE by ~192%, and a reduction of FF by ~35%. The much larger enhancement of J_{sc} over the other parameters indicates a significantly increased concentration of photo-generated charge carriers. Photo-responsiveness of another device slanted at ~45° was also evaluated under a continuous illumination (29.8 mW/cm^2 intensity and 625 nm wavelength) by periodically integrating water droplets on it, as shown in **Fig. 5e**. **Fig. 5f** presents the corresponding temporal photo-responsiveness, revealing that a train of current spikes periodically appears following the periodic water droplets application. **Fig. 5g** corresponds to the blue box in **Fig. 5f**, highlighting the periodic and instant increase of reverse current upon integrating water droplets, measured at -2V. The current reversibly returns to the original value once the droplets subsequently roll down from the sample surface and disappear. We believe that this significant increase of reverse current is a result of the light concentration effect introduced by the integrated water droplets; i.e. the hemispherical water droplet caused by the super-hydrophobic surface enables the in-ward refraction of incident light rays increasing the concentration of photo-generated charge carriers, as schematically illustrated in **Fig. 5h**. The phenomenon is qualitatively consistent with the effects resulting from integrating light concentrating optical lenses on top of photovoltaic cells.[62] Indeed, Li et al. demonstrated significantly enhanced photovoltaic effects by directly integrating water droplets onto the surface of hydrophobic carbon-nanotube photovoltaic cells,[63] which well agrees with the observation in this study. As a control experiment to verify this hypothesis, we prepared for a glass slide with hydrophobic coating and integrated it on top of a $PtTe_2$/Si device. We then integrated water droplets on top of the glass slide/device and performed photovoltaic measurements, mimicking the experiments in **Fig. 5f** and **5g**. As predicated, a significant increase of photocurrent is observed with integrating water droplets (**Fig. S8, ESI†**),

which decisively confirms the super-hydrophobicity enabled light concentration effect.

CONCLUSIONS

In summary, we have developed large-area $PtTe_2$/Si heterojunction devices by directly growing metallic 2D $PtTe_2$ multilayers on p-Si wafers and explored their photovoltaic and photodetection properties. The devices exhibit a comprehensive set of promising Schottky junction characteristics, i.e., large rectification ratio, small ideality factor, high photo sensitivity and small photo response times. Extensive comparisons with previously explored 2D layers-based similar devices confirm their excellence in high-efficiency opto-electrical applications. Furthermore, the devices present improved performances upon integrating water droplets on their surfaces owing to the unusually high hydrophobic nature of 2D $PtTe_2$ layers. This study is believed to greatly broaden the versatility of 2D $PtTe_2$ layers - a relatively unexplored 2D crystal with high electrical conductivity – towards scalable 2D/3D hybrid device applications in a wide range of emerging opto-electronics.

Conflicts of interest

There are no conflicts to declare.

Acknowledgements

Y. J. acknowledges financal supports from the National Science Foundation (CMMI-1728390) (M.S.S., and Y. J.), the Korea Institute of Energy Technology Evaluation and Planning (KETEP) and the Ministry of Trade, Industry & Energy (MOTIE) of the Republic of Korea (No. 20173010013340), and the VPR Advancement of Early Career Researchers award from the University of Central Florida. S.S. and J.A.L. thank Knut och Alice Wallenberg foundation, Kempestiftelserna and Interreg Nord for financial support. S.S. and J.A.L. also thank High Performance Computing Center North (HPC2N), National Supercomputer Center in Linköping (NSC), and the PDC Center for High Performance Computing for allocation of time and resources, through the Swedish National Infrastructure for Computing (SNIC). The authors thank Drs. Putnam and Roy for experimental support in his interfacial transport laboratory and in her next-generation electronics laboratory, respectively.

Notes and references

1. M. Wang, T.-J. Ko, M. S. Shawkat, S. S. Han, E. Okogbue, H.-S. Chung, T.-S. Bae, S. Sattar, J. Gil, C. Noh, K. H. Oh, Y. Jung, J. A. Larsson and Y. Jung, *ACS Appl. Mater. Interfaces*, 2020, **12**, 10839-10851.
2. S. S. Han, J. H. Kim, C. Noh, J. H. Kim, E. Ji, J. Kwon, S. M. Yu, T.-J. Ko, E. Okogbue, K. H. Oh, H.-S. Chung, Y. Jung, G.-H. Lee and Y. Jung, *ACS Appl. Mater. Interfaces*, 2019, **11**, 13598-13607.
3. E. Okogbue, S. S. Han, T.-J. Ko, H.-S. Chung, J. Ma, M. S. Shawkat, J. H. Kim, J. H. Kim, E. Ji, K. H. Oh, L. Zhai, G.-H. Lee and Y. Jung, *Nano Lett.*, 2019, **19**, 7598-7607.
4. Y. Jung, J. Shen, Y. Liu, J. M. Woods, Y. Sun and J. J. Cha, *Nano Lett.*, 2014, **14**, 6842-6849.
5. J. H. Kim, T.-J. Ko, E. Okogbue, S. S. Han, M. S. Shawkat, M. G. Kaium, K. H. Oh, H.-S. Chung and Y. Jung, *Sci. Rep.*, 2019, **9**, 1641.
6. L. Britnell, R. M. Ribeiro, A. Eckmann, R. Jalil, B. D. Belle, A. Mishchenko, Y. J. Kim, R. V. Gorbachev, T. Georgiou, S. V. Morozov, A. N. Grigorenko, A. K. Geim, C. Casiraghi, A. H. C. Neto and K. S. Novoselov, *Science*, 2013, **340**, 1311.
7. T.-J. Ko, S. S. Han, E. Okogbue, M. S. Shawkat, M. Wang, J. Ma, T.-S. Bae, S. B. Hafiz, D.-K. Ko, H.-S. Chung, K. H. Oh and Y. Jung, *Appl. Mater. Today*, 2020, **20**, 100718.
8. G. Fiori, F. Bonaccorso, G. Iannaccone, T. Palacios, D. Neumaier, A. Seabaugh, S. K. Banerjee and L. Colombo, *Nat. Nanotechnol.*, 2014, **9**, 768-779.
9. D. Akinwande, N. Petrone and J. Hone, *Nat. Commun.*, 2014, **5**, 5678.
10. A. Ciarrocchi, A. Avsar, D. Ovchinnikov and A. Kis, *Nat. Commun.*, 2018, **9**, 919.
11. R. A. B. Villaos, C. P. Crisostomo, Z.-Q. Huang, S.-M. Huang, A. A. B. Padama, M. A. Albao, H. Lin and F.-C. Chuang, *npj 2D Mater. Appl.*, 2019, **3**, 2.
12. M. S. Shawkat, H.-S. Chung, D. Dev, S. Das, T. Roy and Y. Jung, *ACS Appl. Mater. Interfaces*, 2019, **11**, 27251-27258.
13. M. S. Shawkat, J. Gil, S. S. Han, T.-J. Ko, M. Wang, D. Dev, J. Kwon, G.-H. Lee, K. H. Oh, H.-S. Chung, T. Roy, Y. Jung and Y. Jung, *ACS Appl. Mater. Interfaces*, 2020, **12**, 14341-14351.
14. W. Zhang, Z. Huang, W. Zhang and Y. Li, *Nano Res.*, 2014, **7**, 1731-1737.
15. J. Qiao, X. Kong, Z.-X. Hu, F. Yang and W. Ji, *Nat. Commun.*, 2014, **5**, 4475.
16. Y. Zhao, J. Qiao, Z. Yu, P. Yu, K. Xu, S. P. Lau, W. Zhou, Z. Liu, X. Wang, W. Ji and Y. Chai, *Adv. Mater.*, 2017, **29**, 1604230.
17. Y. Wang, L. Li, W. Yao, S. Song, J. T. Sun, J. Pan, X. Ren, C. Li, E. Okunishi, Y.-Q. Wang, E. Wang, Y. Shao, Y. Y. Zhang, H.-t. Yang, E. F. Schwier, H. Iwasawa, K. Shimada, M. Taniguchi, Z. Cheng, S. Zhou, S. Du, S. J. Pennycook, S. T. Pantelides and H.-J. Gao, *Nano Lett.*, 2015, **15**, 4013-4018.
18. K. Deng, M. Yan, C.-P. Yu, J. Li, X. Zhou, K. Zhang, Y. Zhao, K. Miyamoto, T. Okuda, W. Duan, Y. Wu, X. Zhong and S. Zhou, *Science Bulletin*, 2019, **64**, 1044-1048.
19. M. S. Bahramy, O. J. Clark, B. J. Yang, J. Feng, L. Bawden, J. M. Riley, I. Marković, F. Mazzola, V. Sunko, D. Biswas, S. P. Cooil, M. Jorge, J. W. Wells, M. Leandersson, T. Balasubramanian, J. Fujii, I. Vobornik, J. E. Rault, T. K. Kim, M. Hoesch, K. Okawa, M. Asakawa, T. Sasagawa, T. Eknapakul, W. Meevasana and P. D. C. King, *Nat. Mater.*, 2018, **17**, 21-28.
20. M. Yan, H. Huang, K. Zhang, E. Wang, W. Yao, K. Deng, G. Wan, H. Zhang, M. Arita, H. Yang, Z. Sun, H. Yao, Y. Wu, S. Fan, W. Duan and S. Zhou, *Nat. Commun.*, 2017, **8**, 257.
21. L. Fu, D. Hu, R. G. Mendes, M. H. Rümmeli, Q. Dai, B. Wu, L. Fu and Y. Liu, *ACS Nano*, 2018, **12**, 9405-9411.
22. H. Ma, P. Chen, B. Li, J. Li, R. Ai, Z. Zhang, G. Sun, K. Yao, Z. Lin, B. Zhao, R. Wu, X. Tang, X. Duan and X. Duan, *Nano Lett.*, 2018, **18**, 3523-3529.
23. E. Okogbue, T.-J. Ko, S. S. Han, M. S. Shawkat, M. Wang, H.-S. Chung, K. H. Oh and Y. Jung, *Nanoscale*, 2020, DOI: 10.1039/D0NR01845G.

24. L. Wang, J. Jie, Z. Shao, Q. Zhang, X. Zhang, Y. Wang, Z. Sun and S.-T. Lee, *Adv. Funct. Mater.*, 2015, **25**, 2910-2919.
25. H. Huang, J. Wang, W. Hu, L. Liao, P. Wang, X. Wang, F. Gong, Y. Chen, G. Wu, W. Luo, H. Shen, T. Lin, J. Sun, X. Meng, X. Chen and J. Chu, *Nanotechnology*, 2016, **27**, 445201.
26. X. Yu, P. Yu, D. Wu, B. Singh, Q. Zeng, H. Lin, W. Zhou, J. Lin, K. Suenaga, Z. Liu and Q. J. Wang, *Nat. Commun.*, 2018, **9**, 1545.
27. C. H. Mak, S. Lin, L. Rogée and S. P. Lau, *J. Phys. D: Appl. Phys.*, 2019, **53**, 065102.
28. H. Tian, A. Hu, Q. Liu, X. He and X. Guo, *Advanced Optical Materials*, 2020, **8**, 1901741.
29. X. Wan, Y. Xu, H. Guo, K. Shehzad, A. Ali, Y. Liu, J. Yang, D. Dai, C.-T. Lin, L. Liu, H.-C. Cheng, F. Wang, X. Wang, H. Lu, W. Hu, X. Pi, Y. Dan, J. Luo, T. Hasan, X. Duan, X. Li, J. Xu, D. Yang, T. Ren and B. Yu, *npj 2D Mater. Appl.*, 2017, **1**, 4.
30. K. Konstantinos and J. A. Larsson, *J. Phys.: Condens. Matter*, 2020.
31. L. Zeng, S. Lin, Z. Lou, H. Yuan, H. Long, Y. Li, W. Lu, S. P. Lau, D. Wu and Y. H. Tsang, *NPG Asia Mater.*, 2018, **10**, 352-362.
32. L.-H. Zeng, Q.-M. Chen, Z.-X. Zhang, D. Wu, H. Yuan, Y.-Y. Li, W. Qarony, S. P. Lau, L.-B. Luo and Y. H. Tsang, *Adv. Sci.*, 2019, **6**, 1901134.
33. C. Xie, L. Zeng, Z. Zhang, Y.-H. Tsang, L. Luo and J.-H. Lee, *Nanoscale*, 2018, **10**, 15285-15293.
34. Z.-X. Zhang, Z. Long-Hui, X.-W. Tong, Y. Gao, C. Xie, Y. H. Tsang, L.-B. Luo and Y.-C. Wu, *The Journal of Physical Chemistry Letters*, 2018, **9**, 1185-1194.
35. Z. Lu, Y. Xu, Y. Yu, K. Xu, J. Mao, G. Xu, Y. Ma, D. Wu and J. Jie, *Adv. Funct. Mater.*, 2020, **30**, 1907951.
36. L.-H. Zeng, D. Wu, S.-H. Lin, C. Xie, H.-Y. Yuan, W. Lu, S. P. Lau, Y. Chai, L.-B. Luo, Z.-J. Li and Y. H. Tsang, *Adv. Funct. Mater.*, 2019, **29**, 1806878.
37. J.-M. Liu, *Photonic devices*, Cambridge University Press, 2009.
38. L. Wang, J.-J. Li, Q. Fan, Z.-F. Huang, Y.-C. Lu, C. Xie, C.-Y. Wu and L.-B. Luo, *J. Mater. Chem. C*, 2019, **7**, 5019-5027.
39. K. Zhou, J. Shen, X. Li, X. Hong, W. Feng, X. Tang, X. Jiang, D. Wei, Y. Chen, X. Liu, Y. Xie, D. Wei and T. Sun, *Physica E: Low-dimensional Systems and Nanostructures*, 2020, **123**, 114147.
40. C. Yim, N. McEvoy, S. Riazimehr, D. S. Schneider, F. Gity, S. Monaghan, P. K. Hurley, M. C. Lemme and G. S. Duesberg, *Nano Lett.*, 2018, **18**, 1794-1800.
41. D. Wu, C. Jia, F. Shi, L. Zeng, P. Lin, L. Dong, Z. Shi, Y. Tian, X. Li and J. Jie, *J. Mater. Chem. A*, 2020, **8**, 3632-3642.
42. L.-H. Zeng, S.-H. Lin, Z.-J. Li, Z.-X. Zhang, T.-F. Zhang, C. Xie, C.-H. Mak, Y. Chai, S. P. Lau, L.-B. Luo and Y. H. Tsang, *Adv. Funct. Mater.*, 2018, **28**, 1705970.
43. D. Wu, Y. Wang, L. Zeng, C. Jia, E. Wu, T. Xu, Z. Shi, Y. Tian, X. Li and Y. H. Tsang, *ACS Photonics*, 2018, **5**, 3820-3827.
44. H. Qiao, Z. Huang, X. Ren, S. Liu, Y. Zhang, X. Qi and H. Zhang, *Advanced Optical Materials*, 2020, **8**, 1900765.
45. Q. Liang, Q. Wang, Q. Zhang, J. Wei, S. X. Lim, R. Zhu, J. Hu, W. Wei, C. Lee, C. Sow, W. Zhang and A. T. S. Wee, *Adv. Mater.*, 2019, **31**, 1807609.
46. S. Hao, J. Zeng, T. Xu, X. Cong, C. Wang, C. Wu, Y. Wang, X. Liu, T. Cao, G. Su, L. Jia, Z. Wu, Q. Lin, L. Zhang, S. Yan, M. Guo, Z. Wang, P. Tan, L. Sun, Z. Ni, S.-J. Liang, X. Cui and F. Miao, *Adv. Funct. Mater.*, 2018, **28**, 1803746.
47. W. Yu, S. Li, Y. Zhang, W. Ma, T. Sun, J. Yuan, K. Fu and Q. Bao, *Small*, 2017, **13**, 1700268.
48. L. Ye, H. Li, Z. Chen and J. Xu, *ACS Photonics*, 2016, **3**, 692-699.
49. R. K. Ulaganathan, Y.-Y. Lu, C.-J. Kuo, S. R. Tamalampudi, R. Sankar, K. M. Boopathi, A. Anand, K. Yadav, R. J. Mathew, C.-R. Liu, F. C. Chou and Y.-T. Chen, *Nanoscale*, 2016, **8**, 2284-2292.
50. X. Zhou, L. Gan, W. Tian, Q. Zhang, S. Jin, H. Li, Y. Bando, D. Golberg and T. Zhai, *Adv. Mater.*, 2015, **27**, 8035-8041.
51. G. W. Mudd, S. A. Svatek, L. Hague, O. Makarovsky, Z. R. Kudrynskyi, C. J. Mellor, P. H. Beton, L. Eaves, K. S. Novoselov, Z. D. Kovalyuk, E. E. Vdovin, A. J. Marsden, N. R. Wilson and A. Patanè, *Adv. Mater.*, 2015, **27**, 3760-3766.
52. X. Wang, P. Wang, J. Wang, W. Hu, X. Zhou, N. Guo, H. Huang, S. Sun, H. Shen, T. Lin, M. Tang, L. Liao, A. Jiang, J. Sun, X. Meng, X. Chen, W. Lu and J. Chu, *Adv. Mater.*, 2015, **27**, 6575-6581.
53. G. Su, V. G. Hadjiev, P. E. Loya, J. Zhang, S. Lei, S. Maharjan, P. Dong, P. M. Ajayan, J. Lou and H. Peng, *Nano Lett.*, 2015, **15**, 506-513.
54. J. Mao, Y. Yu, L. Wang, X. Zhang, Y. Wang, Z. Shao and J. Jie, *Adv. Sci.*, 2016, **3**, 1600018.
55. R. Zhuo, L. Zeng, H. Yuan, D. Wu, Y. Wang, Z. Shi, T. Xu, Y. Tian, X. Li and Y. H. Tsang, *Nano Res.*, 2019, **12**, 183-189.
56. F. Wang, Z. Wang, K. Xu, F. Wang, Q. Wang, Y. Huang, L. Yin and J. He, *Nano Lett.*, 2015, **15**, 7558-7566.
57. S. R. Tamalampudi, Y.-Y. Lu, R. K. U, R. Sankar, C.-D. Liao, K. M. B, C.-H. Cheng, F. C. Chou and Y.-T. Chen, *Nano Lett.*, 2014, **14**, 2800-2806.
58. M. Sajjad, N. Singh, M. De Bastiani, S. De Wolf and U. Schwingenschlögl, *physica status solidi (RRL) – Rapid Research Letters*, 2019, **13**, 1900328.
59. K. K. N. Simon M. Sze, *Physics of Semiconductor Devices*, Wiley, New Jersey.
60. A. P. S. Gaur, S. Sahoo, M. Ahmadi, S. P. Dash, M. J. F. Guinel and R. S. Katiyar, *Nano Lett.*, 2014, **14**, 4314-4321.
61. P. K. Chow, E. Singh, B. C. Viana, J. Gao, J. Luo, J. Li, Z. Lin, A. L. Elías, Y. Shi, Z. Wang, M. Terrones and N. Koratkar, *ACS Nano*, 2015, **9**, 3023-3031.
62. M. Alves, A. Pérez-Rodríguez, P. J. Dale, C. Domínguez and S. Sadewasser, *Journal of Physics: Energy*, 2019, **2**, 012001.
63. X. Li, Y. Jung, K. Sakimoto, T.-H. Goh, M. A. Reed and A. D. Taylor, *Energy Environ. Sci.*, 2013, **6**, 879-887.

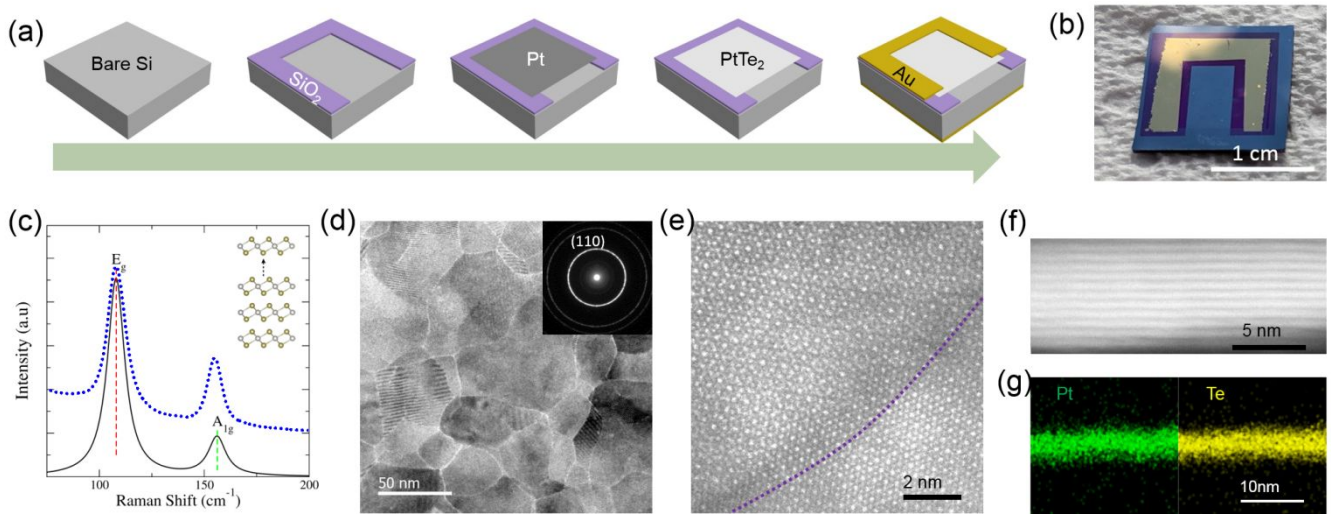

Fig. 1. (a) Schematic illustration of sequential steps for fabricating $PtTe_2$/Si heterojunction devices. (b) Image of a complete $PtTe_2$/p-Si Schottky junction device. (c) Raman spectroscopy characterization of few-layer 2D $PtTe_2$, comparing the theoretically calculated spectrum (black solid line) with the experimentally determined one (blue dotted line). (d) Plane-view STEM image of 2D $PtTe_2$ layers and the corresponding SAED pattern in the inset. (e) Plane-view HR-STEM image revealing two neighboring stitching grains, separated by the grain boundary (purple dotted curve). (f) Cross-sectional HR-STEM image of 2D $PtTe_2$ multilayers. (g) Cross-sectional STEM–EDS elemental mapping images corresponding to (f).

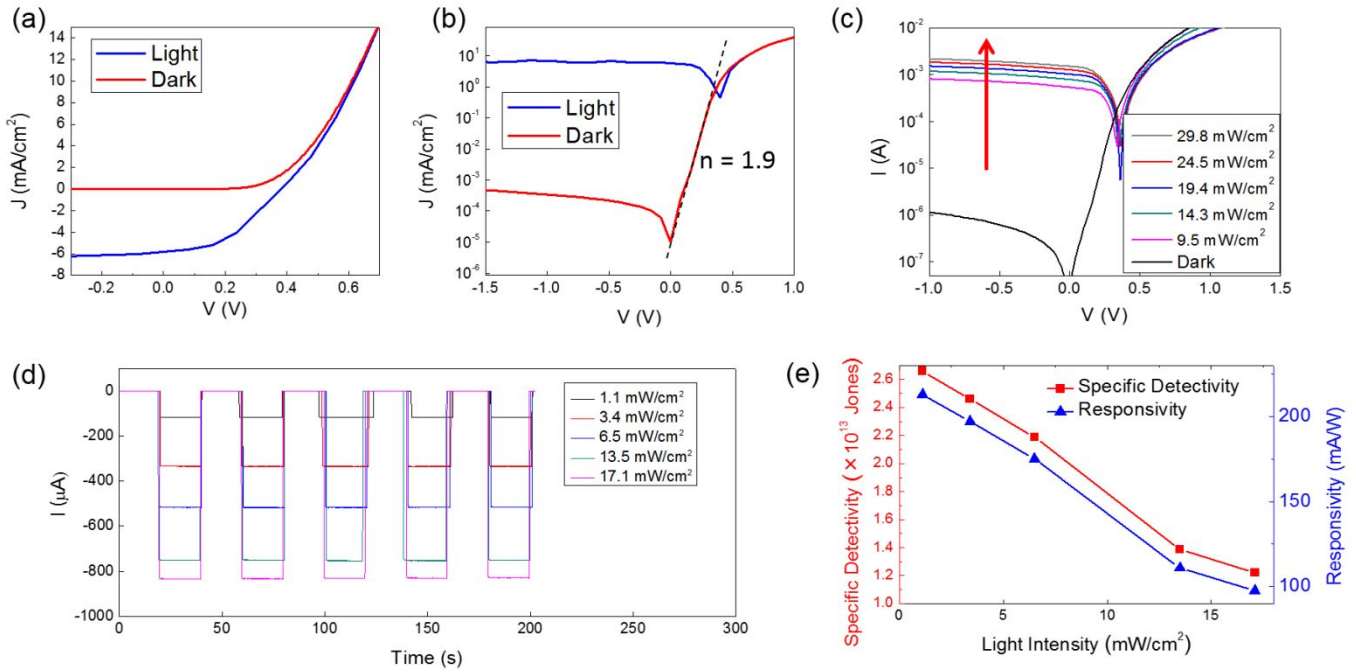

Fig. 2. (a-c) Photovoltaics of $PtTe_2$/p-Si devices prepared with Pt of 4.5 nm thickness; (a) J–V characteristics in dark (red) and under illumination (blue), and (b) the corresponding presentation in a semi-log scale. (c) I-V characteristics of another device in a semi-log scale measured under 625 nm illumination of varying intensity. (d,e) Photo-responsiveness measured at zero external bias; (d) Temporal response of a device under 625 nm illumination of varying intensity. (e) Light intensity-dependent specific detectivity (red) and responsivity (blue) of the same device in (d)

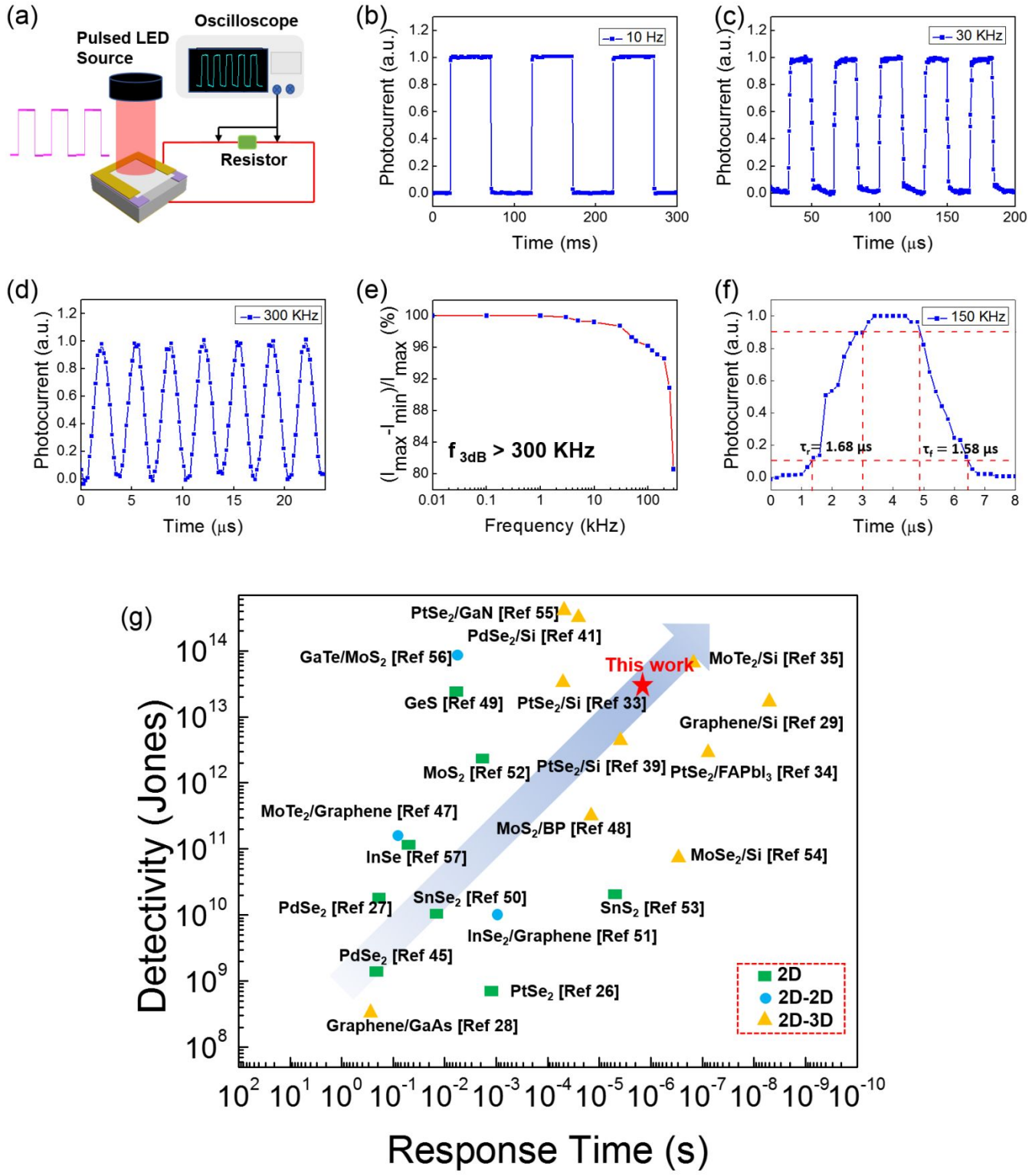

Fig. 3. (a) Schematic illustration of the experimental setup for recording the temporal photo-responsiveness of $PtTe_2$/p-Si devices under periodically-pulsed 625 nm illumination. (b-d) Temporal photo-responsiveness of a device measured at varying illumination frequencies of; (b) 10 Hz, (c) 30 kHz, and (d) 300 kHz. (e) Relative balance, $(I_{max}-I_{min})/I_{max}$, of the same device as a function of illumination modulation frequency revealing a 3-dB cutoff frequency of > 300 kHz. (f) Magnified view of photo-switching characteristics obtained at 150 kHz clarifying rise (τ_r) and fall (τ_f) times. (g) Comparison of photo-responsiveness performances between the $PtTe_2$/p-Si device in this work vs. other 2D, 2D-2D, and 2D-3D heterojunction devices in previous reports.

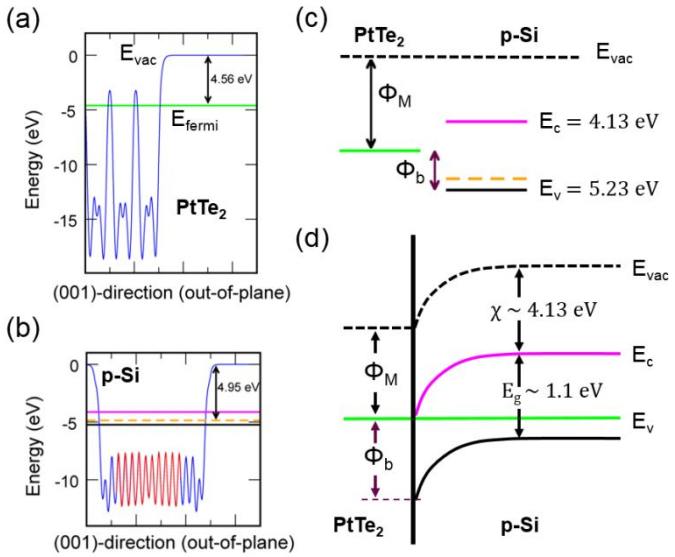

Fig. 4. (a) PAEP diagram of few layer 2D $PtTe_2$ and its calculated work function, (4.56 eV, green line) with vacuum level at 0 eV. (b) Determination of the work function of p-Si (4.95 eV, orange line) and band offsets by superimposing the PAEP of bulk Si on that of the slab and calibrating the vacuum level to 0 eV. (c) Energy band diagrams for 2D $PtTe_2$ and p-Si that form a p-type Schottky contact upon interfacing. (d) Band bending diagram revealing a presence of $PtTe_2$/p-Si Schottky barrier whose height is determined to be 0.67 eV (violet line).

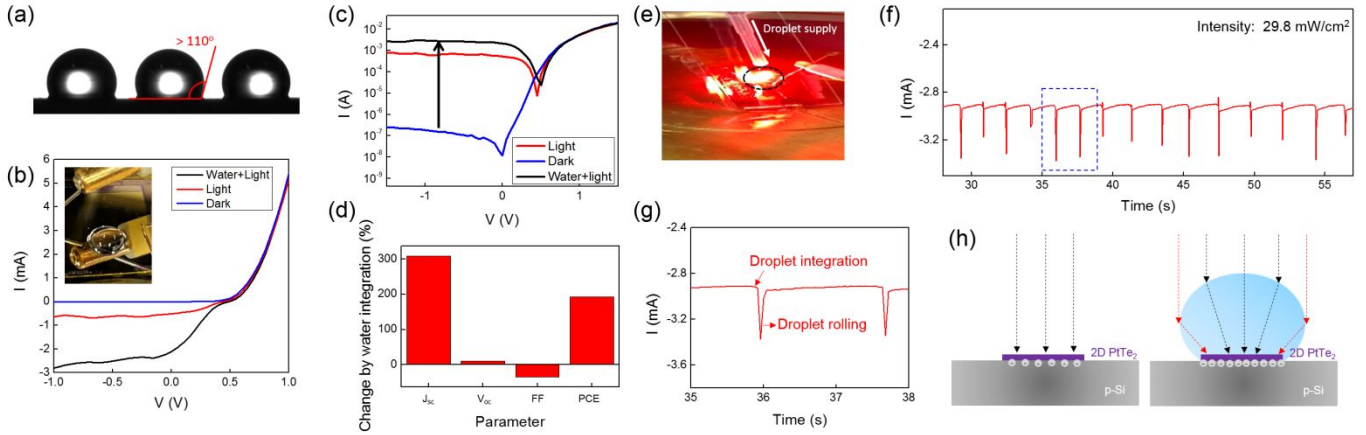

Fig. 5. (a) Image of water droplets integrated on a $PtTe_2$/p-Si device. (b) I-V characteristics of a $PtTe_2$/p-Si device in dark (blue), under illumination (red), and after integrating the water droplet shown in the inset (black). (c) I-V characteristics in a semi-log scale corresponding to (b). (d) Change of photovoltaic parameters induced by the water droplet integration in (b) and (c). (e) Integration of water droplets on a $PtTe_2$/p-Si device slanted at ~ 45° under continuous illumination from a 625 nm LED source at an intensity of 29.8 mW/cm^2. (f) Temporal current obtained from the device in (e) with a periodic integration of water droplets at an interval of ~ 1.6 sec. (g) Enlarged view of the blue dotted region in (f) highlighting the current change by the droplet integration and rolling-off due to gravity. (h) Schematic illustration of the increased concentration of photo-generated carriers by the light concentration effect.

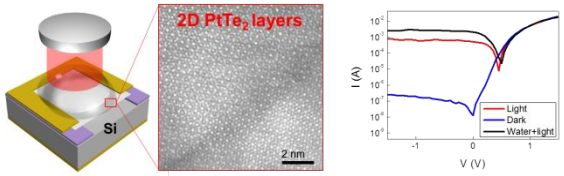

Novel photodetectors based on large-area 2D $PtTe_2$/silicon vertical-junctions exhibit ultra-fast photo-response, high sensitivity, and water-droplet driven photovoltaic enhancement.